Optimized Molecular Aggregation *via* Incorporating Fluorinated unit in the Polymer Donor for 17.3% Efficiency Organic Solar Cells

Qing Guo,[a, c] Ji Lin,[a] Xingliang Dong,[a] Lei Zhu,[b] Xia Guo,*[, a] Feng Liu,[b] Maojie Zhang,*[, a]

[a] College of Chemistry, Chemical Engineering and Materials Science, Soochow University, Suzhou 215123, China

E-mail: zmj2008@iccas.ac.cn (M. J. Zhang); guoxia@iccas.ac.cn (X. Guo)

[b] Frontiers Science Center for Transformative Molecules, In-situ Center for Physical Science, and Center of Hydrogen Science, School of Chemistry and Chemical Engineering, Shanghai Jiao Tong University, Shanghai 200240, P. R. China.

[c] Henan Institute of Advanced Technology, Zhengzhou University, Zhengzhou, 450003, China.

Corresponding Author

* E-mail: zmj2008@iccas.ac.cn (M. J. Zhang); guoxia@iccas.ac.cn (X. Guo)

Abstract: Regulating molecular aggregation state via chemical modification of photovoltaic materials to optimize the blend morphology is an effective and challenging strategy to improve the photovoltaic performance of organic solar cells (OSCs). In this work, we demonstrate a random terpolymerization strategy by incorporating 1,3-bis(5-bromo-4-fluorothiophen-2-yl)-5,7-bis(2-ethylhexyl)-4H,8H-benzo[1,2-c:4,5-c']bisthiophene-4,8-dione (BFT, 30 mol%) unit with fluorinated π-bridges into the molecular backbone of PM6 and develop a terpolymer PF1. Benefiting from the strong electronegativity of fluorine atom and noncovalent interaction of F---S, the energy levels, molecular ordering, and aggregation properties of the polymer donors are precisely regulated. Notably, in the active layer film based on PF1: Y6, the π-π stacking distance can reduce to 3.51 Å, which is significantly smaller than that of PM6:Y6 (3.65 Å) and boosts the effective exciton dissociation and charge transport, thereby effectively optimize the photovoltaic properties of the related devices. As a result, the PF1:Y6-based OSCs achieved a power conversion efficiency (PCE) of up to 17.3%, which is much higher than that of

the controlled OSCs based on PM6:Y6 (PCE=16.2%). These results demonstrate high-efficiency OSCs enabled by regulating molecular aggregation via terpolymerization strategy.

Keywords: organic solar cells; molecular aggregation; terpolymer; noncovalent interactions; power conversion efficiencies

Introduction

Organic solar cells (OSCs) as a promising renewable energy-harvesting technology have been attracted the increasing attention due to their certain highly desired advantages such as low cost, lightweight, flexible and roll-to-roll manufacturing.[1-5] In the past few years, the development of nonfullerene acceptors (NFAs) based on acceptor-donor-acceptor (A-D-A) structure has contributed to the rapid improvement of the power conversion efficiency (PCE) of OSCs. Specially, the recent development of the A-DA'D-A structured Y6 and its derivative acceptors based on electron-deficient core has significantly improved the PCE over 17%. [6-12]

The photovoltaic performance of OSCs is strongly dependent on the blend morphology of active layer. An optimum morphology with well-defined bicontinuous interpenetrating network and nano-scale phase separation is a key factor for efficient exciton dissociation and better charge extraction to achieve higher short-circuit current density (J_{SC}) and fill factor (FF), and then further improve the PCE of OSCs.[13-15] Considerable efforts have been devoted to morphology optimization. On the one hand, device engineering, *via* either one or a combination of two or more processing and strategies to modify the morphology, such as thermal or solvent vapor annealing,[16-17] additives,[18-19] ternary blends,[20-22] and modification of interlayer,[23] is an effective way. On the other hand, modifying molecular packing and aggregation of donor and acceptor materials also plays an important role in optimizing morphology of active layer to improve the photovoltaic performance of OSCs.[24-26]

At present, the top-performing OSCs have delivered over 17% PCEs, which is attributed to the discovery of the novel acceptor Y6.[6-12, 27-28] Among them, PM6:Y6 is a classical system, which

exhibits barrierless free charge generation, leading to high performance.[29] However, the J_{SC} and FF of PM6:Y6-based OSCs is limited due to the relatively low and unbalanced charge transport caused by the insufficient morphology.[6] Based on this, researchers conducted a series of studies to optimize the morphology of blend films in order to further improve the photovoltaic efficiency.[17, 19-21, 27, 30] For example, Zhang *et al*. incorporated a third component BTTzR with high crystallinity into the host PM6:Y6 blend to construct ternary OSCs, leading to the optimized morphology, which contributed to the enhanced and balanced charge transport, and thus the improved J_{SC} and FF.[31] Besides, optimizing the solubility and intermolecular packing of Y6 via the modification of the alkyl chains such as branching strategy is another effective way to tune the morphology of active layer and improve the photovoltaic performance of corresponding OSCs.[32-33]

Apart from these, the aggregation of polymer donors is one of the critical factors determining the morphology of blends. According to the reported literature, polymers with moderately strong aggregation is beneficial to construct ideal nanomorphology, which is necessary to increase charge generation, transport and extraction, and reduce the energy loss.[34-35] Terpolymeriaztion strategy has been proved effective in optmizing photovoltaic performance of polymer donors.[36-38] For instance, in 2020, Zhang et. al. developed a terpolymer donor PM6-Tz20 by incorporating the third 5,5′-dithienyl-2,2′-bithiazole unit into the PM6 backbone to tailor the molecular orientation, aggregation properties and optimize the morphology, yielding an improved device efficiency of 17.6%.[39] Incorporating heteroatom is an effective method to promote aggregation of donors due to the enhanced planarity of molecule caused by intramolecular interactions.[40-42] Among the various species of heteroatom, fluorine holds a large proportion due to its unique advantages such as the similar Van der Waals atoms radius (≈ 147 pm) with hydrogen atom (≈ 120 pm) and the strongest electronegativity.[43] Hence, in this work, we incorporated fluorinated unit 1,3-bis(5-bromo-4-fluorothiophen-2-yl)-5,7-bis(2-ethylhexyl)-4H,8H-benzo[1,2-c:4,5-c']bisthiophene-4,8-dione (BFT, 30 mol%) into the molecular backbone of PM6 by simple random terpolymerization and develop a novel terpolymer donor PF1. Compared to the PM6, the terpolymer PF1 show deeper energy levels, slightly red-shifted absorption,

enhanced planarity, and improved crystallinity and aggregation. Moreover, blended with Y6, the PF1-based blend film shows optimized morphology with well-developed nanoscale interpenetrating network and enlarged fiber width, leading to higher exciton dissociation, improved charge transport and extraction, and lower charge recombination. As a result, the PF1:Y6-based OSCs achieved a high PCE of 17.3% with simultaneously enhanced open-circuit voltage (V_{OC}) of 0.87 V, J_{SC} of 26.3 mA cm^{-2} and FF of 0.76, which is much higher than that of the controlled OSCs based on PM6:Y6 (PCE=16.2%, V_{OC}=0.85 V, J_{SC}=25.8 mA cm^{-2} and FF=0.74). These results indicate that optimizing aggregation of polymers by properly incorporating fluorinated unit is an effective strategy for developing highly efficient OSCs.

Results and Discussion

The BFT monomers was synthesized and purifies according to previously reported procedures.[44] The new terpolymer donors PF1 and PF2 with 30 mol% and 50 mol% of BFT, respectively, were synthesized *via* random polymerization of three monomers (BDT, BDD, and BFT) based on Still coupling reaction (as shown in Scheme 1). The parent alternating copolymer PM6F were also synthesized as the reference polymer. All the polymers show good solubility in common organic solvents, such as chloroform and chlorobenzene. The number average molecular weight (M_n) and polydispersity index (PDI) of all polymers were determined via high-temperature gel permeation chromatography (GPC) with 1,2,4-trichlorobenzene as the eluent. The results displayed in Table 1 indicate all polymers have similar M_n and PDI. Besides, thermogravimetric analyses (TGA) suggest that all polymers possess excellent thermal stability with decomposition temperature (T_d, defined as the temperature with a 5% weight loss) over 410 ºC (as shown in Fig. S1, Supporting Information, SI).

In order to investigate the influences of the BFT unit on the molecular geometry and frontier molecular orbits of polymers, molecular simulations were performed using density functional theory (DFT) at the B3LYP 6-31G** level. According to the calculated results, the distance between neighboring S and F atoms is 2.95 Å, far shorter than the sums of the S and F van der Waals radii (3.71

Å), indicating the existence of noncovalent F---S interaction between the fluorinated thiophene in BFT and BDT units. As a result, introducing BFT units leads to a decreased dihedral angle in the conjugated backbone. Besides, the wave function distributions of the highest occupied molecular orbitals (HOMOs) and the lowest unoccupied molecular orbitals (LUMOs) displayed in Fig. 1b indicate an enhanced orbital delocalization with the incorporation of BFT units. The results suggest that introducing BFT units will improve planarity and enhance conjugation of the backbone in polymers, which is beneficial for molecular aggregation and hole mobilities. Furthermore, the incorporation of BFT units results in down-shifted energy levels due to the electron-deficient property of fluorine and the deeper HOMO levels of terpolymers are expected to have higher V_{OC}.

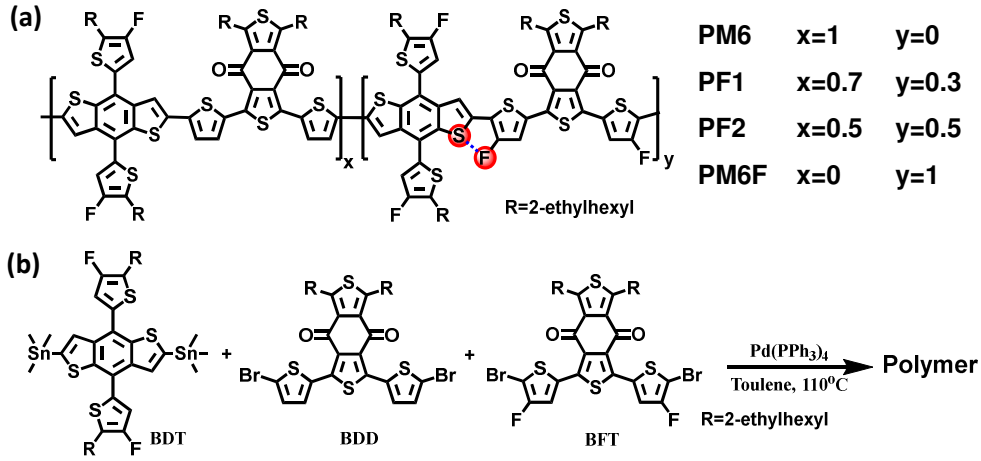

Scheme 1. (a) Molecular structures and (b) synthetic routes of the polymers.

The normalized ultraviolet-visible (UV-vis) absorption spectra of polymers in film state and solution are shown in Fig. 1c and Fig. S3 (SI), respectively, and the related data are listed in Table 1. All the polymers exhibit strong and broad absorption in the range of 400-700 nm. The gradually red-shifted absorption edges are observed in the polymers with the increase of the BFT content. The optical bandgaps (E_g) evaluated from the film absorption edges of the PM6, PF1, PF2, and PM6F are 1.84, 1.81, 1.79 and 1.78 eV, respectively. The absorption characterization for the four blend films were further measured and illustrated in Fig S3b. As shown, the combination of donor and acceptor provides a rather complementary absorption, which covers the range from 400 to 900 nm for all the blend films. We also measured the temperature-dependent UV-vis absorption spectra of polymers in chlorobenzene (Fig. S3, SI). With the increase of temperature, the polymers tend to disaggregate, as reflected in a significant

blue-shifted absorption with distinct spectral features, such as the disappearance of a 0-0 transition at ≈ 620 nm. These results suggest that the polymers possess strong aggregation property effect in the solution state. The electronic energy levels of the polymers were measured by electrochemical cyclic voltammetry (CV). The HOMO energy levels were estimated from the onset oxidation potentials and it was found that the HOMO energy levels of the polymers decrease slightly as the proportion of BFT unit in the polymer increases. These results are derived from the strong electron withdrawing effect of fluorine atoms. The LUMO levels of PM6, PF1, PF2, and PM6F are -3.63, -3.71, -3.78, -3.88 eV, respectively, according to E_g and the HOMO energy levels. The energy levels diagram of the four polymers and Y6 are shown in Fig. 1d. The CV results are consistent with the DFT simulation, and the gradually deeper HOMO levels could contribute to the higher V_{OC}.

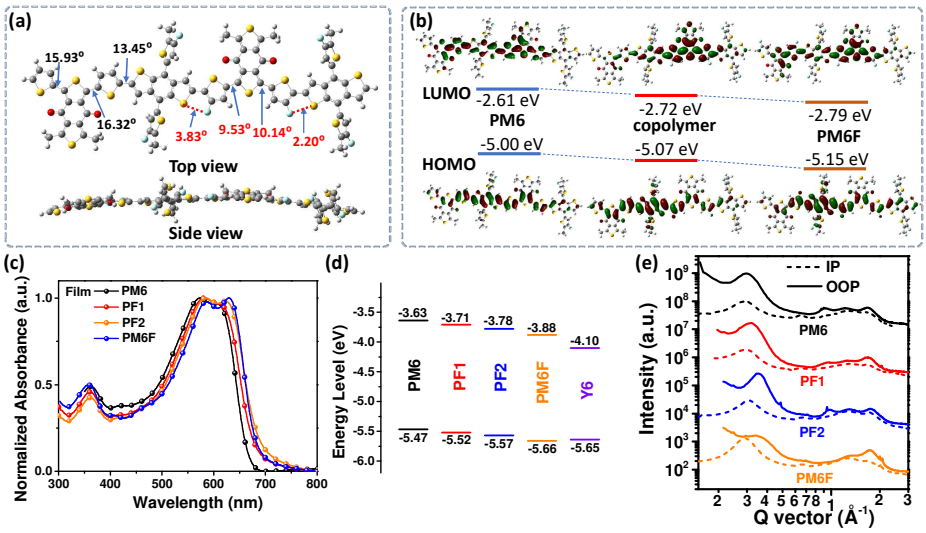

Fig. 1 (a) Simulated chemical geometry of the molecular model for the copolymer with a BDD:BFT ratio of 1:1; (b) Molecular energy levels and wave-function distributions of the frontier orbits for the polymer models; (c) UV-vis absorption spectra of the polymer in the film; (d) Energy levels of the polymers; (e) Extracted 1D profiles along the IP and OOP directions from the 2D GIWAXS patterns.

Table 1. Molecular weight, optical bandgap, and molecular energy levels of the polymers.

Polymers	Mn (kDa)	PDI	E_g (eV)	HOMO (eV)	LUMO (eV)
PM6	21.5	2.47	1.84	-5.47	-3.63
PF1	24.6	2.15	1.81	-5.52	-3.71
PF2	20.5	2.47	1.79	-5.57	-3.78
PM6F	22.8	2.48	1.78	-5.66	-3.88

Grazing-incidence wide-angle X-ray scattering (GIWAXS) measurements were conducted to investigate the effect of the third BFT unit on the orientation and packing of the polymer donors.[45]

The 2D patterns of neat polymer films are shown in Fig S4. The corresponding intensity profiles in the out-of-plane (OOP) direction and in-plane (IP) direction are presented in Fig. 1e. And the detailed results are collected in Table S1 and S2. As demonstrated, the (010) peaks of PM6, PF1, PF2, and PM6F were located at 1.68, 1.69, 1.76 and 1.76 $Å^{-1}$, respectively, indicating the gradually tighter π–π stacking with the increased proportion of BFT unit in the polymer (*d*-spacing of 3.74, 3.72, 3.57, 3.57 Å, respectively). The crystal coherence lengths (CCLs) were calculated according to the Scherrer equation (CCL = 1.8π/FWHM, where FWHM refers to full width at half-maximum of the peaks in the intensity profile).[46] As shown in Table S4, the CCLs of π–π stacking along OOP direction were calculated to be 17.67, 17.67, 17.13, and 18.24 Å for PM6, PF1, PF2, and PM6F, respectively. The tighter π–π stacking and greater CCL are favorable for charge transport. It is noted that PF1 has a moderate crystal size with the CCL of 80.78 Å in the IP direction, which is larger than 70.69 Å for PM6 and smaller than 94.25 Å for PM6F. The enhanced aggregation of terpolymer PF1, compared with PM6, corresponds to the improved planarity caused by the noncovalent F---S interaction. These results indicate that rationally controlled stoichiometry of the third component provides an access to tune the aggregation of polymers for further improving their photovoltaic performance.

OSCs based on these four polymers and Y6 were fabricated by the same processes with a conventional device configuration of indium tin oxide (ITO)/poly(3,4-ethylenedioxythiophene):poly (styrenesulfonate) (PEDOT:PSS)/ active layer/ perylene diimide functionalized with amino N-oxide (PDINO)/ Al. The detailed fabrication processes were demonstrated in the SI. The current density-voltage (*J*-*V*) curves and related photovoltaic parameters of the optimized devices were displayed in Fig. 2a and summarized in Table 2**,** respectively. And the detail data of the optimization process were shown in Table S3-S6. With increasing BFT content of the polymers, the OSCs display gradually improving V_{OC} values from 0.85 to 0.90 V in the optimized devices, as the result of the gradually reducing HOMO energy levels. Besides, the J_{SC} and FF of the devices show a tendency of increasing first and then decreasing. As a result, compared to the PM6-based OSCs with the PCE of 16.2%, J_{SC} of 25.8 mA cm^{-2} and FF of 0.74, the PF1-based devices achieved the improved PCE of 17.3% with the best J_{SC} of 26.3

mA cm^{-2} and FF of 0.76 among the four devices, indicating that introducing fluorinated unit BFT into PM6 polymer backbone to develop high-performance polymer donor is effective. However, when the proportion of BFT is increased further, i.e., PF1 is replaced with PF2, the photovoltaic performance of the devices reduced significantly: the PCE is 14.1% with a lower J_{SC} of 22.9 mA cm^{-2} and FF of 0.70. In contrast, the PM6F-based devices give the lowest efficiency of 9.7% with the lowest J_{SC} and FF, which may be due to the unmatched energy levels and excessive aggregation. Thus, precise control of the content of the third component BFT is the key to achieve the corresponding high-efficiency OSCs.

The external quantum efficiency (EQE) spectra of the optimized devices were measured and shown in Fig. 3c. All the devices show a wide respond range from 300 to 900 nm. Compared to the PM6-based device, the PF1-based device shows higher EQE value in the range of 700-900 nm, which correlates well with the enhanced J_{SC}. With further increasing proportion of BFT, the EQE values of devices tend to decrease, which comes from the increased geminate charge recombination and insufficient photoinduced hole transfer from the acceptor material Y6 to polymer donor.[47-48] In addition, the J_{SC} values calculated by integrating the EQE spectra matches well with the values obtained from *J*-*V* measurements (as shown in Table 2).

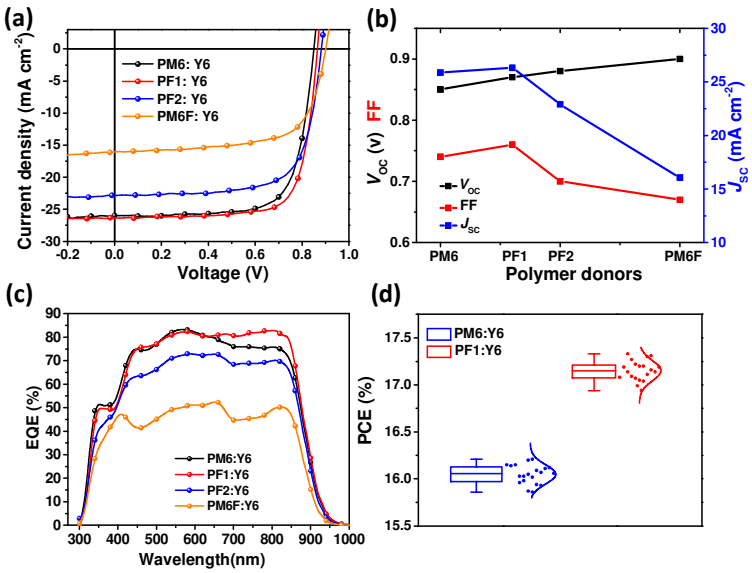

Fig. 2 (a) *J*-*V* curves for the optimized devices, under the illumination of AM1.5G, 100 mW cm^{-2}; (b) V_{OC}, FF and J_{SC} parameters for the four devices; (c) EQE plots for the optimized devices; (d) Statistical histograms of the PCEs measured for the polymer:Y6-based devices.

Table 2. Detailed photovoltaic parameters of the optimized devices with different polymers under AM 1.5 G illumination (100 mW cm^{-2}).

Devices	V_{OC} (V)	J_{SC} (mA cm^{-2})[a)]	FF	PCE (%)[b)]
PM6:Y6	0.85	25.8 (25.3)	0.74	16.2 (16.0±0.2)
PF1:Y6	0.87	26.3 (26.1)	0.76	17.3 (17.1±0.2)
PF2:Y6	0.88	22.9 (22.3)	0.70	14.1 (14.0±0.1)
PM6F:Y6	0.90	16.1 (15.5)	0.67	9.7 (9.5±0.2)

[a)] The integral J_{sc} from the EQE curves in brackets. [b)] The average values and standard deviations of the device parameters based on 20 devices are shown in brackets.

In order to explore the reasons of the improved photovoltaic performance caused by the introduction of the third unit BFT into PM6 backbone, crystalline, morphological and structural properties of the blend films were investigated by GIWAXS, atomic force microscopy (AFM) and transmission electron microscopy (TEM). GIWAXS was employed to study the molecular orientation and crystallinity for blend films. As shown in Fig. 3, blend films summarize diffraction features from component materials. For all the blend films, the π–π stacking peaks (010) appeared in the OOP direction, indicating the preferred face-on orientation, which is favorable for vertical charge transport. As for the blend film diffraction signals were quite close to Y6 in the OOP direction, and therefore it is hard to clearly separate them out. In spite of this, similar with the observed trend in neat films, the stacking of the blend films tends to higher with increased proportion of BFT in the polymer backbone (the detailed results are collected in Tables S1 and S2, SI). The π–π stacking distance of PM6, PF1, PF2 and PM6F-based blend films is 3.65, 3.51, 3.51 and 3.49 Å, respectively. The value of 3.51Å is among the smallest π-π stacking distance in Non-fullerene OSCs,[44, 49-50] which can facilitate charge transport. Besides, the changes in CCL values of (100) peak in the IP direction and (010) peak in the OOP direction are largely in parallel with the BFT content. With the increase of BFT unit content, the conjugated backbone planarity increases, resulting in the better molecular ordering and the increase of crystal size in the blend film. It should be noted that the CCL of PF2:Y6 and PM6F:Y6 raises significantly in the IP direction, which may increase the phase separation.

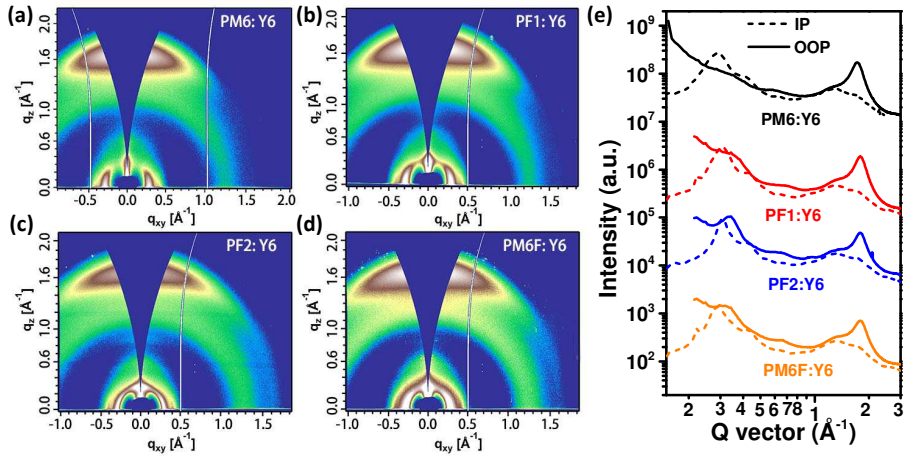

Fig. 3 2D-GIWAXS scattering patterns of blend films of (a) PM6:Y6 (b) PF1:Y6 (c) PF2:Y6 and (d) PM6F:Y6; (e) Extracted 1D profiles along the IP and OOP directions from the 2D GIWAXS patterns.

AFM and TEM measurements were carried out to investigate the morphological properties of the four blend films.[51-52] As shown in Fig. 4, the AFM images of PM6, PF1, PF2 and PM6F blends showed gradually increasing root-mean-square (RMS) roughness values of 1.01, 1.05, 2.24 and 2.54 nm, likely due to the increased levels of crystallinity as demonstrated in GIWAXS results. These results imply that improving the content of BFT unit may help to form large donor domains, contributing to extensive phase separation in the blend films, evidenced by the phase images of AFM and TEM images as shown in Fig. 4. In PM6:Y6 and PF1:Y6 films, distinct fibrillar bi-continuous interpenetrating network are observed. However, PF2 and PM6F blend films display the obvious dark and light domains, demonstrating the extensive phase separation. Compared to the PM6-based blend film, it is notable that the PF1 blend film exhibits an enlarged fiber width with a well-developed nanoscale interpenetrating network, which is beneficial for charge carrier transport and suppressive bimolecular recombination, in good agreement with the higher J_{SC} and FF.

In addition, to further explore the fundamental origin of the morphological difference, the miscibility between donor and acceptor was investigated by measuring the surface tension (γ) based on the contract angle of materials (Fig. S5, SI). Herein, we qualitatively compared the donor:acceptor miscibility according to Flory–Huggins interaction parameter (χ), based on the empirical equation $\chi = K(\sqrt{\gamma_{donor}} - \sqrt{\gamma_{acceptor}})^2$ (where K is a constant).[53-54] From the viewpoint of polymer thermodynamics, a lower χ value equates to greater molecular miscibility. Notably, the increase of BFT

content can improve the surface energies, and the increased $(\sqrt{\gamma_{donor}} - \sqrt{\gamma_{acceptor}})^2$ from 0.19 to 0.58, indicating the reduced miscibility between polymer and Y6, which are in agreement with the results of AFM and TEM.

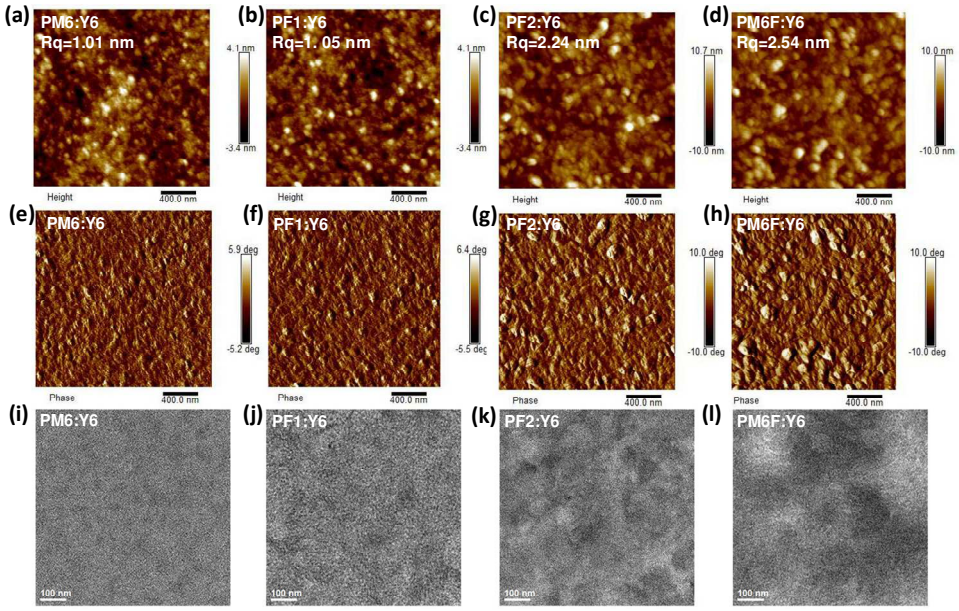

Fig. 4 AFM images of (a), (e) PM6:Y6; (b), (f) PF1:Y6; (c), (g) PF2:Y6 and (d), (h) PM6F:Y6 blend films; TEM images of (i) PM6:Y6; (j) PF1:Y6; (k) PF2:Y6 and (l) PM6F:Y6 blend films.

To better understand the influence of morphological optimization of active layer caused by the third unit BFT of the polymer donor on its photovoltaic performance, the exciton dissociation probabilities $P(E,T)$, charge recombination, and charge mobilities of the related OSCs were investigated. Fig. 5a shows the plots of photocurrent (J_{ph}) versus effective voltage (V_{eff}) curves for the optimized devices.[55-56] J_{ph} is determined as $J_{ph} = J_L - J_D$, where J_L and J_D are the current density under illumination and in the dark. V_{eff} is defined by $V_{eff} = V_0 - V_a$, where V_0 is the voltage at which $J_{ph} = 0$ and V_a is the applied voltage. For the PM6, PF1, and PF2-based devices, the J_{ph} increases in proportion to the V_{eff} and rapidly achieves a plateau at 0.3-0.5 V and the PF1-based devices gives the highest saturated photocurrent (P_{sat}) value of 26.9 mA cm^{-2}. However, the photocurrent in the PM6F-based device shows field-dependent dissociation of exciton in saturation regime, suggesting the severe geminate charge recombination, which agrees with the inferior efficiency of the OSC. The $P(E,T)$ is calculated from the ratio of J_{ph}/J_{sat}. For the PM6, PF1, PF2 and PM6F-based devices, the $P(E,T)$ values are 98.4%, 98.7% 94.5% and 89.3% under short-circuit condition, while the corresponding $P(E,T)$

values under maximum power output condition are 89.1%, 89.4%, 80.2% and 69.3%, respectively. The higher $P(E,T)$ values of the PF1-based device indicate the excellent exciton dissociation and charge collection efficiencies, which are consistent with the improved J_{SC} and FF of the device.

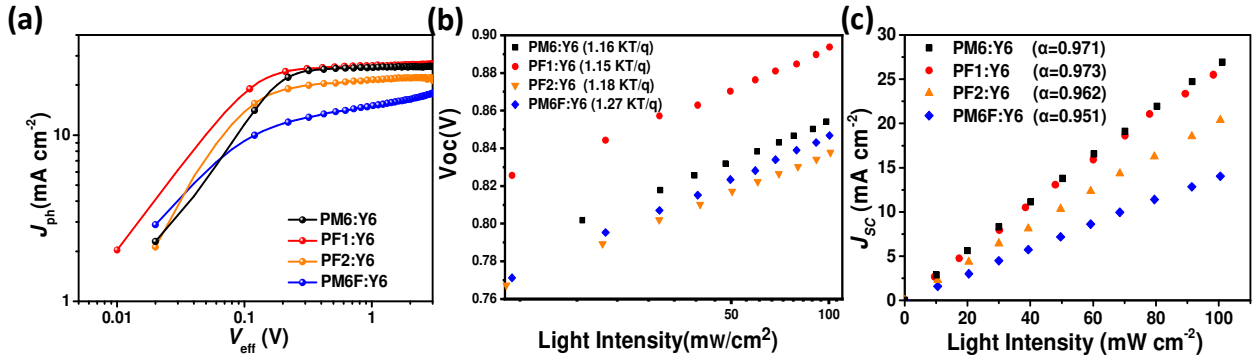

Fig. 5 (a) J_{ph} versus V_{eff} and (b) V_{OC} and (c) J_{SC} versus P_{light} curves for the optimized devices.

Light intensity dependence of OSCs performance was investigated to understand the charge recombination behavior. The relationship between V_{OC} and light intensity (P_{light}) is as follows: V_{OC} □ log(P_{light}). The signature of trap-assisted recombination depicts a stronger dependence of V_{OC} on log(P_{light}) with a slope of 2 *KT/q*. As shown in Fig. 5b, the slope values for PM6:Y6, PF1:Y6, PF2:Y6 and PM6F:Y6-based films are 1.16, 1.15, 1.18 and 1.27 *KT/q*, respectively. The small slopes indicate that bimolecular recombination dominates for the four devices. And the smallest value for PF1:Y6-based film indicated the weakest trap-assisted recombination. The J_{SC} on incident P_{light} can be described as J_{SC} □ P_{light}^{α}, where α reflects the information of the bimolecular recombination.[57-58] Herein, the α values of the PM6:Y6 and PF1:Y6-based devices were calculated to be 0.971 and 0.973, respectively, both of which were closely to 1, indicating the negligible bimolecular recombination. Besides, the slightly higher (more close to 1) α value of the PF1-based OSCs is also beneficial to achieve higher FF. As the proportion of BFT unit further increases, the values of α declined to be 0.962 and 0.951 for the PF2:Y6 and PM6F:Y6-based devices. The gradually enhanced bimolecular recombination usually leads to lower FF and device performance.

In addition, the hole and electron mobilities (μ_h *and* μ_e) were measured by the space charge limited current (SCLC) method to investigate the charge transporting behavior of the devices.[59-60] As shown in Fig. S6 and Table S7 (SI), the μ_h and μ_e for PM6:Y6, PF1:Y6, PF2:Y6 and PM6F:Y6-based

films are 4.75×10^{-4} / 5.66×10^{-4}, 6.43×10^{-4} / 5.72×10^{-4}, 3.46×10^{-4} / 4.32×10^{-4} and 4.91×10^{-4} / 3.31×10^{-4} $cm^2\ V^{-1}\ s^{-1}$, and the corresponding μ_h /μ_e ratios are 0.84, 1.12, 0.80, 1.49, respectively. The higher μ_h *and* μ_e values and more balanced μ_h /μ_e ratio of PF1:Y6-based film contribute to the higher J_{SC} and FF.

Conclusion

In conclusion, we developed a novel high-performance terpolymer donor PF1 by incorporating fluorinated unit BFT (30 mol%) into PM6 backbone. Benefiting from the improved planarity of PF1 caused by the noncovalent interaction of F---S, the molecular ordering and aggregation properties of the polymer are precisely regulated, resulting in the optimized active layer morphology, which boosts the processes of effective exciton dissociation and charge transport, thereby effectively optimize the photovoltaic performance of the related devices. Blending with Y6 acceptor, the PF1-based OSC achieved a much higher PCE of 17.3% with simultaneously significantly enhanced V_{OC} of 0.87 V, J_{SC} of 26.3 mA cm^{-2} and FF of 0.76 than the PM6-based OSC (PCE=16.2%, V_{OC}=0.85 V, J_{SC}=25.8 mA cm^{-2} and FF=0.74. This study indicates that optimizing aggregation of the polymer donors by properly incorporation of the fluorinated unit is an effective strategy for achieving highly efficient performance of the OSCs.

Acknowledgements

This work was supported by National Natural Science Foundation of China (NSFC) (No. 51773142, 51973146, 51973110 and 21905102), Jiangsu Provincial Natural Science Foundation (Grant No. BK20190099), the Collaborative Innovation Center of Suzhou Nano Science & Technology, the Priority Academic Program Development of Jiangsu Higher Education Institutions. The X-ray data were acquired at beamlines 7.3.3 at the Advanced Light Source, which is supported by the Director, Office of Science, Office of Basic Energy Sciences, of the U.S. Department of Energy under Contract No. DE-AC02-05CH11231.

[1] J. Hou, O. Inganas, R. H. Friend, F. Gao, O. Inganäs, R. H. Friend, F. Gao, Nat. Mater. 17 (2018) 119.

[2] D. Di Carlo Rasi, R. A. J. Janssen, Adv. Mater. 31 (2019) 1806499.

[3] O. Ostroverkhova, Chem. Rev.116 (2016) 13279.

[4] P. Cheng, G. Li, X. Zhan, Y. Yang, Nat. Photonics 12 (2018) 131.

[5] S. Dai, X. Zhan, Adv. Energy Mater. 8 (2018) 1800002.

[6] J. Yuan, Y. Zhang, L. Zhou, G. Zhang, H.-L. Yip, T.-K. Lau, X. Lu, C. Zhu, H. Peng, P. A. Johnson, M. Leclerc, Y. Cao, J. Ulanski, Y. Li, Y. Zou, Joule 3 (2019) 1140.

[7] Q. Liu, Y. Jiang, K. Jin, J. Qin, J. Xu, W. Li, J. Xiong, J. Liu, Sci. Bull. 65 (2020) 272.

[8] Y. Cui, H. Yao, J. Zhang, K. Xian, T. Zhang, L. Hong, Y. Wang, Y. Xu, K. Ma, C. An, C. He, Z. Wei, F. Gao,J. Hou, Adv. Mater. 32 (2020) 1908205.

[9] F. Liu, L. Zhou, W. Liu. Z. Zhou, Q. Yue, W. Zheng. R. Sun, W. Liu, S. Xu. H. Fan, L. Feng, Y. Yi, W. Zhang, X. Zhu, Adv. Mater. 33 (2021) 2100830.

[10] Z. Luo, R. Ma, T. Liu, J. Yu, Y. Xiao, R. Sun, G. Xie, J. Yuan, Y. Chen, K. Chen, G. Chai, H. Sun, J. Min, J. Zhang, Y. Zou, C. Yang, X. Lu, F. Gao, H. Yan, Joule 4 (2020) 1236.

[11] R. Ma, T. Liu, Z. Luo, Q. Guo, Y. Xiao, Y. Chen, X. Li, S. Luo, X. Lu, M. Zhang, Y. Li, H. Yan, Sci. China Chem. 63 (2020) 325.

[12] Y. Cui, Y. Xu, H. Yao, P. Bi, L. Hong, J. Zhang, Y. Zu, T. Zhang, J. Qin, J. Ren, Z. Chen, C. He, X. Hao, Z. Wei, J. Hou, Adv. Mater. 33 (2021) 2102420.

[13] W. Tress, A. Merten, M. Furno, M. Hein, K. Leo, M. Riede, Adv. Energy Mater. 3 (2013) 631.

[14] Y. Huang, E. J. Kramer, A. J. Heeger, G. C. Bazan, Chem. Rev. 114 (2014) 7006.

[15] Q. Fan, W. Su, Y. Wang, B. Guo, Y. Jiang, X. Guo, F. Liu, T. P. Russell, M. Zhang, Y. Li, Sci. China Chem. 61 (2018) 531.

[16] Q. Guo, X. Zhu, X. Dong, Q. Zhu, J. Fang, X. Guo, W. Ma, M. Zhang, Y. Li, J. Mater. Chem. A, 7 (2019) 24366.

[17] L. Zhu, M. Zhang, G. Zhou, T. Hao, J. Xu, J. Wang, C. Qiu, N. Prine, J. Ali, W. Feng, X. Gu, Z. Ma, Z. Tang, H. Zhu, L. Ying, Y. Zhang, F. Liu, Adv. Energy Mater. 10 (2020) 1904234.

[18] R. Yu, H. Yao, Z. Chen, J. Xin, L. Hong, Y. Xu, Y. Zu, W. Ma, J. Hou, Adv. Mater. 31 (2019) 1900477.

[19] L. Liu, Y. Kan, K. Gao, J. Wang, M. Zhao, H. Chen, C. Zhao, T. Jiu, A. K. Jen, Y. Li, Adv. Mater. 32 (2020) 1907604.

[20] K. Li, Y. Wu, Y. Tang, M. A. Pan, W. Ma, H. Fu, C. Zhan, J. Yao, Adv. Energy Mater. 9 (2019) 1901728.

[21] Q. An, J. Wang, W. Gao, X. Ma, Z. Hu, J. Gao, C. Xu, M. Hao, X. Zhang, C. Yang, F. Zhang, Sci. Bull. 65 (2020) 538.

[22] X. Guo, Q. Fan, C. Cui, Z. Zhang, M. Zhang, Acta Phys.-Chim. Sin. 34 (2018) 1279.

[23] J. Wang, Z. Zheng, D. Zhang, J. Zhang, J. Zhou, J. Liu, S. Xie, Y. Zhao, Y. Zhang, Z. Wei, J. Hou, Z. Tang, H. Zhou, Adv. Mater. 31 (2019) 1806921.

[24] T. Wang, R. Sun, M. Shi, F. Pan, Z. Hu, F. Huang, Y. Li, J. Min, Adv. Energy Mater. 10 (2020) 200590.

[25] Q. Guo, R. Ma, J. Hu, Z. Wang, H. Sun, X. Dong, Z. Luo, T. Liu, X. Guo, X. Guo, H. Yan, F. Liu, M. Zhang, Adv. Funct. Mater. 30 (2020) 2000383.

[26] X. Liu, X. Wang, Y. Xiao, Q. Yang, X. Guo, C. Li, Adv. Energy Mater. 10 (2020) 1903650.

[27] J. Song, C. Li, L. Zhu, J. Guo, J. Xu, X. Zhang, K. Weng, K. Zhang, J. Min, X. Hao, Y. Zhang, F. Liu, Y. Sun, Adv. Mater. 31 (2019) 1905645.

[28] T. Yan, W. Song, J. Huang, R. Peng, L. Huang, Z. Ge, Adv. Mater. 31 (2019) 1902210.

[29] L. Perdigon-Toro, H. Zhang, A. Markina, J. Yuan, S. M. Hosseini, C. M. Wolff, G. Zuo, M. Stolterfoht, Y. Zou, F. Gao, D. Andrienko, S. Shoaee, D. Neher, Adv. Mater. 32 (2020) 1906763.

[30] Q. Liu, J. Fang, J. Wu, L. Zhu, X. Guo, F. Liu, M. Zhang, Chinese J Chem. 39 (2021) 1941.

[31] Q. Liu, Y. Wang, J. Fang, H. Liu, L. Zhu, X. Guo, M. Gao, Z. Tang, L. Ye, F. Liu, M. Zhang, Y. Li, Nano Energy 32 (2021) 105963.

[32] Y. Cui, H. Yao, J. Zhang, K. Xian, T. Zhang, L. Hong, Y. Wang, Y. Xu, K. Ma, C. An, C. He, Z. Wei, F. Gao, J. Hou, Adv. Mater. 32 (2020) 1908205.

[33] K. Jiang, Q. Wei, J. Y. L. Lai, Z. Peng, H. K. Kim, J. Yuan, L. Ye, H. Ade, Y. Zou, H. Yan, Joule 3 (2019) 3020.

[34] H. Fu, Z. Wang, Y. Sun, Angew. Chem. Int. Ed. 58 (2019) 4442.

[35] T. Heumueller, W. R. Mateker, I. T. Sachs-Quintana, K. Vandewal, J. A. Bartelt, T. M. Burke, T. Ameri, C. J. Brabec, M. D. McGehee, Energy Environ. Sci. 7 (2014) 2974.

[36] D. Dang, D. Yu, E. Wang, Adv. Mater. 31 (2019) 1807019.

[37] X. Huang, L. Zhang, Y. Cheng, J. Oh, C. Li, B. Huang, L. Zhao, J. Deng, Y. Zhang, Z. Liu, F. Wu, X. Hu, C. Yang, L. Chen, Y. Chen, Adv. Funct. Mater. 31 (2021) 2108634.

[38] L. Zhou, L. Meng, J. Zhang, C. Zhu, S. Qin, I. Angunawela, Y. Wan, H. Ade, Y. Li, Adv. Funct. Mater. 31 (2021) 2109271.

[39] X. Guo, Q. Fan, J. Wu, G. Li, Z. Peng, W. Su, J. Lin, L. Hou, Y. Qin, H. Ade, L. Ye, M. Zhang, Y. Li, Angew. Chem. Int. Ed. 60 (2021) 2322.

[40] H. Huang, Q. Guo, S. Feng, C. Zhang, Z. Bi, W. Xue, J. Yang, J. Song, C. Li, X. Xu, Z. Tang, W. Ma, Z. Bo, Nat. Commun. 10 (2019) 3038.

[41] M. Saito, T. Fukuhara, S. Kamimura, H. Ichikawa, H. Yoshida, T. Koganezawa, Y. Ie, Y. Tamai, H. D. Kim, H. Ohkita, I. Osaka, Adv. Energy Mater. 10 (2020) 1903278.

[42] H. Huang, L. Yang, A. Facchetti, T. J. Marks, Chem. Rev. 117 (2017) 10291.

[43] Q. Fan, U. A. Mendez-Romero, X. Guo, E. Wang, M. Zhang, Y. Li, Chem. Asian. J. 14 (2019) 3085.

[44] Z. Fei, F. D. Eisner, X. Jiao, M. Azzouzi, J. A. Rohr, Y. Han, M. Shahid, A. S. R. Chesman, C. D. Easton, C. R. McNeill, T. D. Anthopoulos, J. Nelson, M. Heeney, Adv. Mater. 30 (2018) 1705209.

[45] P. Muller-Buschbaum, Adv. Mater. 26 (2014) 7692.

[46] D.-M. Smilgies, J. Appl. Crystallogr. 42 (2009) 1030.

[47] S. K. Pal, T. Kesti, M. Maiti, F. Zhang, O. Inganas, S. Hellstrom, M. R. Adersson, F. Oswald, F. Langa, T. Osterman, T. Pascher, A. Yartsev, V. Sundstrom, J. Am. Chem. Soc, 132 (2010) 12440.

[48] N. Schopp, V. V. Brus, J. Lee, G. C. Bazan, T. Q. Nguyen, Adv. Energy Mater, 10 (2020) 2002760.

[49] B. Fan, M. Li, D. Zhang, W. Zhong, L. Ying, Z. Zeng, K. An, Z. Huang, L. Shi, G. C. Bazan, F. Huang, Y. Cao, ACS Energy Lett. 5 (2020) 2087.

[50] J. Song, L. Ye, C. Li, J. Xu, S. Chandrabose, K. Weng, Y. Cai, Y. Xie, P. O'Reilly, K. Chen, J. Zhou, Y. Zhou, J. M. Hodgkiss, F. Liu, Y. Sun, Adv. Sci. 7 (2020) 2001986.

[51] F. Zhao, C. Wang, X. Zhan, Adv. Energy Mater. 8 (2018) 1703147.

[52] B. Guo, W. Li, X. Guo, X. Meng, W. Ma, M. Zhang, Y. Li, Adv. Mater. 29 (2017) 1702291.

[53] J. Comyn, Int J Adhes. Adhes. 12 (1992) 145.

[54] M. Kim, J. Lee, S. B. Jo, D. H. Sin, H. Ko, H. Lee, S. G. Lee, K. Cho, J. Mater. Chem. A 4 (2016) 15522.

[55] S. Li, L. Ye, W. Zhao, H. Yan, B. Yang, D. Liu, W. Li, H. Ade, J. Hou, J. Am. Chem. Soc. 140 (2018) 7159.

[56] L. Lu, W. Chen, T. Xu, L. Yu, Nat. Commun. 6 (2015) 7327.

[57] P. W. M. Blom, V. D. Mihailetchi, L. J. A. Koster, D. E. Markov, Adv. Mater. 19 (2007) 1551.

[58] S. R. Cowan, A. Roy, A. J. Heeger, Phys. Rev. B 82 (2010) 245207.

[59] J. Chen, G. Li, Q. Zhu, X. Guo, Q. Fan, W. Ma, M. Zhang, J. Mater. Chem. A 7 (2019) 3745.

[60] X. Guo, M. Zhang, J. Tan, S. Zhang, L. Huo, W. Hu, Y. Li, J. Hou, Adv. Mater. 24 (2012) 6536.